

## **A novel design of solid oxide electrolyzer for hydrogen generation and storage integrating magnesium hydride bed - A dynamic simulation study**

Chen Bin<sup>1</sup>, Haoran Xu<sup>1</sup>, Houcheng Zhang<sup>1,2</sup>, Peng Tan<sup>1</sup>, Weizi Cai<sup>1</sup>, Meng Ni<sup>1,\*</sup>

<sup>1</sup> Building Energy Research Group, Department of Building and Real Estate  
The Hong Kong Polytechnic University, Hung Hom, Kowloon, Hong Kong, China

<sup>2</sup> Department of Microelectronic Science and Engineering, Ningbo University,  
Ningbo 315211, China

### **Abstract**

This paper proposed the proof-of-concept of a novel solid oxide steam electrolyzer with the in-situ hydrogen storage capacity by integrating a magnesium hydride (MH) section with proton-conducting solid oxide electrolysis cell (SOEC) section. By dynamic simulation, it takes 1950 seconds to fully charge the MH section with a 56% H<sub>2</sub> storage efficiency without any flow recirculation, when the electrolyzer is operated at 1.4 volts and 4 atm, yielding a current density of 4956.40 A/m<sup>2</sup>. The evolution of temperature, H<sub>2</sub> partial pressure and reacted a fraction of Mg powder through the charging process were analyzed, founding the exothermic H<sub>2</sub> adsorption process of MH section can enhance the performance of the electrolysis process of SOEC section. The effects of operating parameters including operating pressure, electrolysis voltage, and cooling air temperature were identified by sensitivity studies. Results show that it is beneficial to operate the electrolyzer at elevated pressure for shorter adsorption time and higher H<sub>2</sub> storage efficiency; Increasing the operating voltage can shorten the adsorption time, but lower H<sub>2</sub> storage efficiency; An optimal cooling air temperature was be found at 510K when the electrolyser operated at 1.4 V and 4 atm.

**Keywords:** solid oxide electrolysis cell; metal hydride; hydrogen storage; dynamic simulation

# 1 Introduction

Hydrogen is a clean renewable energy carrier, yielding only H<sub>2</sub>O when releasing its chemical energy via combustion or electrochemically conversion. This merit is attracting great attention to the research on hydrogen production and utilization when environment issues are becoming urgent worldwide.

However, hydrogen conventionally is produced from fossil fuels by steam reforming process, which will inevitably generate greenhouse gas emissions and pollutions [1]. Thermochemical and photocatalytic splitting of water for hydrogen both have drawbacks in low energy efficiency [2] [3] [4] [5]. Alternatively, water electrolysis process using renewable energy can serve as a sustainable solution, as there are nearly no extra CO<sub>2</sub> emissions when the electricity power is from the wind, solar, redundant grid power, and waste heat.

Solid oxide electrolyzer cell (SOEC) operated at high temperature (ca.600°C~800°C) nowadays are receiving much attentions in the area of water electrolysis [6-9], due to its high efficiency, and capability of recovering renewable electricity and heat, which is more advantageous than the low temperature Nafion-based proton exchange membrane (PEM) electrolyser. However, there still exists a lot of technical issues unaddressed in the commercialization of SOEC. Besides material degradation and cost issues, the hydrogen storage remains a challenge, hindering the application of SOEC in the renewable energy system.

## 1.1 A short review of Metal hydride bed for hydrogen storage

Hydrogen, the lightest element, behaves as a low volumetric energy carrier at ambient pressure, thus requiring large compression work to improve its volumetric energy density in the case of high pressure storage (35 MPa ~70 MPa) [10]. Other popular

storage methods can be classified to liquid storage and adsorption storage. Liquid storage also demands large amount energy to liquefy the hydrogen (boiling point: 21.2 K at 1 atm) in the liquefaction process (eg. Linde cycle) [11]. Besides, leakage problems caused by permeation and evaporation are making the liquid storage and pressure storage not energy efficient options. Differently, the adsorption storage method adsorbs the hydrogen molecules/atoms onto solid surface of porous storage medium or chemically fix the hydrogen by the reaction of hydrogen with metal to form hydrogen hydrides [12], thus it shows less energy requirement, high reversibility, and low safety risk due to the moderate storage pressure and temperate. More importantly, most storage media excels in the volumetric/gravimetric capacity compared to compressed H<sub>2</sub> gas or liquid hydrogen. For example, pure carbon nanotube/nanofibers (CNT/CNF) can uptake hydrogen by physisorption at a theoretical capacity of 7.7wt% [13] or even up to 67 wt% using CNF at 11.2 MPa in disputable experimental works [14]. The metal organic framework (MOF) is another kind of physisorption media, the porous cubic crystalline structure of which can uptake 1wt% storage at room temperature and 20 bar or 4.5 wt% at 78K and 0.8 bar [15].

Metal hydrides, which is usually solid metal-hydrogen compounds, is considered as a good candidate for hydrogen storage media in high mobility applications, promising to fulfill the 6.5 wt% hydrogen target set by the U.S. Department of Energy. Generally, metals (eg. Li, Na, Mg, Ti) or intermetallic compounds (LaNi<sub>5</sub>, Mg<sub>2</sub>Ni) can react with the hydrogen to form metal hydrides ( $\beta$ -phase) when the hydrogen atoms behave like a metal element and dissolved into the metal (solid-solution,  $\alpha$ -phase) [12]. The  $\alpha$ - $\beta$  transition process can be described by the pressure-concentration-temperature plot and Van't Hoff law (Fig. 1), from which a flat charging & discharging pressure plateau can be observed. Additional heat is required to maintain the exothermic absorption process.

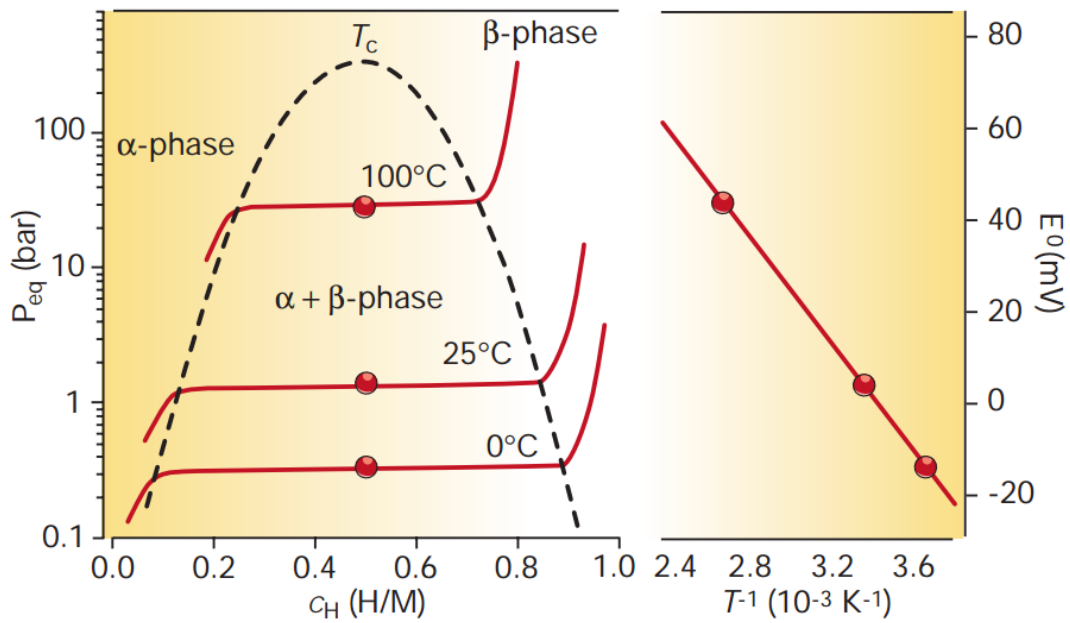


**Fig. 1** Pressure–concentration–temperature plot (left) and a Van't Hoff curve (right) for LaNi<sub>5</sub>. The vertical axes indicate the corresponding hydrogen pressure and the equivalent electrochemical potential [16]

Presently, the metal hydride has been integrated with fuel cells in energy power systems as the hydrogen desorbed from hydride is of high purity, suitable for the fuel cell application. Besides, the waste heat from fuel cells can be employed to the hydride bed to improve the overall system energy efficiency using proper thermal integration methods. T. Førde et al developed a 1.2 kW PEM fuel cell stack (1.5 bar) fuelled by Ce-modified LaNi<sub>5</sub>H<sub>6</sub> hydride(15 bar), using water loop recirculation to recycle the waste heat of PEM fuel cell to heat up the hydride tank [17]. They also employed a PEM electrolyzer working at 15 bar to charging the hydride tank. Rizzi et al integrated a LaNi<sub>4.8</sub>Al<sub>0.2</sub> tank as the hydrogen supplier with a PEM fuel cell stack, yielding 4.8 kWh after one-time discharge of the hydride [18]. Baptiste et al set up the first SOFC based CHP system combined with MgH<sub>2</sub> tank (operated at 2.7 atm) as the hydrogen supplier for a 1kWe SOFC stack with thermal integration [19]. R. Urbanczyk

et al integrated a 260W high temperature PEM fuel cell (HT-PEM) with complex metal hydride ( $\text{Na}_3\text{AlH}_4$  doped with  $\text{TiCl}_3$ ) at a working condition of  $200^\circ\text{C}$  and 10 atm [20].

To the best of author's knowledge, there are very few existing studies on using metal hydride to storage the hydrogen from SOEC as standalone components[21], and there is no report on the SOEC-metal hydride(SOEC-MH) system with pressure integration, by which the pressurized SOEC works at the same pressure with metal hydride bed in a compact single component. In this paper, An  $\text{Mg}/\text{MgH}_2$  metal hydride bed is chosen to be integrated inside a tubular pressurized SOEC, serving for the in-situ hydrogen storage. Both in-situ thermal and pressure integration are achieved in this SOEC-MH electrolyser and mathematically studied in terms of dynamic performance and storage efficiency.

The selection of  $\text{Mg}/\text{MgH}_2$  is owing to its advantageous storage properties compared to other metal hydrides as follows:

- (i) The theoretic highest hydrogen weight capacity (7.7 wt%) in all metal hydride system. [22]
- (ii) Low cost, due to the abundant Mg sources.
- (iii) Low adsorption/desorption pressure at high temperature (ca. 2 atm at  $300^\circ\text{C}$ ). [23]
- (iv) High adsorption/desorption temperature (ca. $300^\circ\text{C}$ ), suitable for integration with SOEC. [23]

## 2 Concept and design

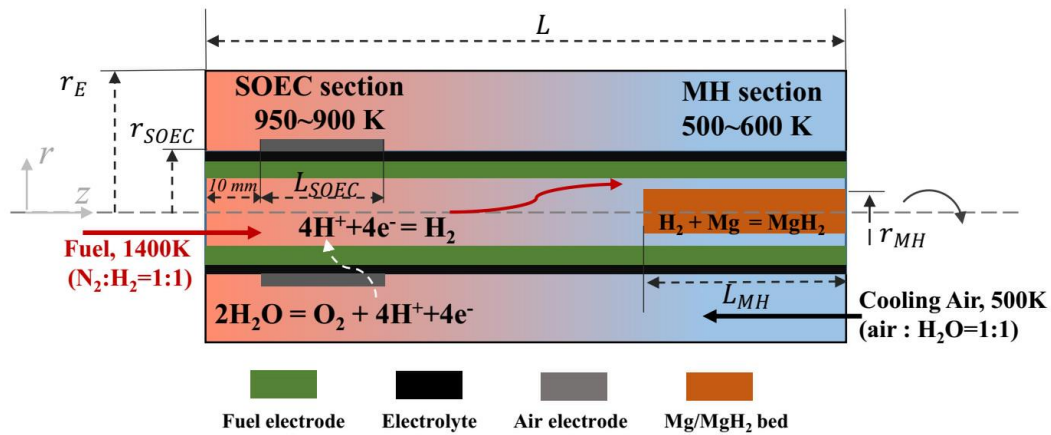


**Fig. 2** Schematic of the tubular electrolyser with the SOEC section and MH section at base case operation (scaled for better display)

The tubular electrolyser design is schematically shown in Fig. 2, which can be divided into two parts: the SOEC section and MH section. In the base case operation, the SOEC section is operated in high temperature region (ca. 900 K ~ 950 K), while the MH section is defined to be the low temperature region (ca. 500 K ~ 600 K), in which the cylinder-shaped MH bed is set along the concentric axis. Such temperature gradient distribution is maintained by counter flow configuration: the inlet fuel flow of 1400 K inside the tube and the cooling air flow of 500 K outside the tube. The working pressure of tubular electrolyser is 4 atm, corresponding to an  $\text{H}_2$  partial pressure ( $p_{\text{H}_2}$ ) at ca. 2 atm initially, so that the adsorption temperature would be near the temperature of MH section according to the thermodynamic equilibrium diagram between Mg and MgH<sub>2</sub> (Fig. 3) [23].

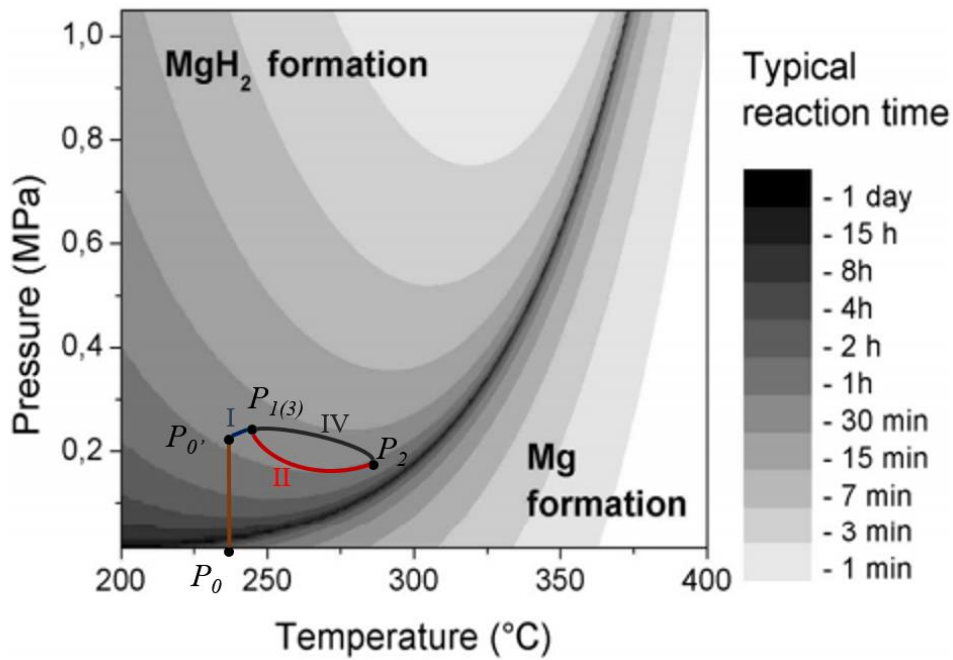
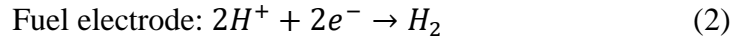
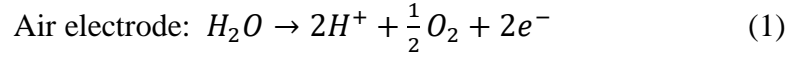


**Fig. 3** The H<sub>2</sub> pressure-temperature diagram of the phase equilibrium between Mg/MgH<sub>2</sub>. Reaction time is denoted with the grey color level [23].

The SOEC is set to be a cathode support proton-conducting SOEC based on BZCY electrolyte with the configuration of Ni-BZCY || BaCe<sub>0.5</sub>Zr<sub>0.3</sub>Y<sub>0.2</sub>O<sub>3-δ</sub> (BZCY) || Sm<sub>0.5</sub>Sr<sub>0.5</sub>CoO<sub>3-δ</sub> (SSC)-BZCY. As a result, the steam would be supplied to the cooling flow outside the tube, so that it is not necessary to concern the degradation of the Mg/MgH<sub>2</sub> bed due to the reaction between Mg and steam (generation of MgO).

Initially, in the base case operation, the fuel flow should be pure N<sub>2</sub> flow in case of undesired Mg consumption so that the Mg bed is in a stand-by condition (Point P<sub>0</sub> in Fig. 3). When the electrolyzer starts to work, the fuel gas flow is switched to the carrier gas with N<sub>2</sub>: H<sub>2</sub>=1:1 in volume (P<sub>0</sub> → P<sub>0'</sub>) and an electrolysis voltage (1.4V) is applied (P<sub>0'</sub> → P<sub>1</sub>). H<sub>2</sub>O in the cooling air would be electrolyzed, generating oxygen carried away by the cooling flow as Eq. 1, and protons to be conducted towards the fuel flow through the proton conducting electrolyte. The protons on the fuel electrode side would receive electrons, generating hydrogen in the fuel flow as Eq. 2.



Thereafter, the hydrogen-rich fuel flow will pass through the porous Mg bed in the MH section with the hydrogen absorbed in the product (MgH<sub>2</sub>) to some extent:



The heat generated from SOEC and hydrogen adsorption process will increase the Mg/MgH<sub>2</sub> bed temperature, therefore the Mg/MgH<sub>2</sub> bed will approach point  $P_2$  via route II and then goes back towards the full charged point(via route III to Point  $P_3$ ). As the switch process and voltage loading are much faster than the adsorption process, there would be very limited amount MgH<sub>2</sub> formed during this two process ( $P_0 \rightarrow P_0' \rightarrow P_1$ ). This dynamic simulation starts from  $P_1$  and assumes that the reacted fraction of Mg material ( $X$ ) at  $P_1$  is 0.

General geometric parameters for the tubular electrolyser and setups are referred from a typical tubular SOEC prototype [24] as summarized in Table. 1. Inlet temperature and flux are adjusted for desired temperature distribution.

Table. 1 The geometry parameters of SOEC section and MH section and the operating parameters used in the base case.

Parameters	Value
Electrolyser length, $L$	80 mm
Radius of SOEC-MH electrolyser, $r_E$	5.1 mm
<b>SOEC section</b>	
Length, $L_{SOEC}$	16 mm
Radius of SOEC tube radius, $r_{SOEC}$	2.1 mm
Air electrode thickness	30 $\mu$ m

Fuel electrode thickness	308 $\mu\text{m}$
Electrolyte thickness	12 $\mu\text{m}$
<b>MH section</b>	
Length, $L_{MH}$	13 mm
Radius, $r_{MH}$	1 mm
<b>Operating conditions (base case)</b>	
Air inlet temperature, $T_{fuelin}$	1400 K
Fuel inlet temperature, $T_{airin}$	500 K
Operating pressure, $p_{op}$	4 atm
Air flow	23 sccm, Air: H <sub>2</sub> O=1:1 in volume
Fuel flow	40 sccm, N <sub>2</sub> :H <sub>2</sub> =1:1 in volume
SOEC electrolysis voltage, $V_{op}$	1.4 V

### 3 Research objectives

The design briefed above provides a compact solution to convert electricity to hydrogen of fixed form. The hydrogen production will be transportation friendly and of high quality (purity, volumetric energy density, and safety). However, the feasibility of this design needs to be carefully studied since the MH section is very sensitive to its operation conditions including pressure and temperature, while the SOEC is sensitive to the temperature.

Therefore, this simulation work is intended to firstly study the base case operation performance of the novel SOEC-MH electrolyzer as a feasibility demonstration, then the effects of the operation conditions would be analyzed in terms of three sensitivity studies on pressure, voltage, and cooling air inlet temperature, respectively.

The development of the model could be a design tool for the further practical configuration of the tubular solid oxide electrolyser in terms of size, arrangement of sections, sophisticated thermal integration: temperature settings controllable by gas flow rate and pressure settings.

#### 4 Model development

A dynamic 2D-axisymmetric model is built to simulate the SOEC-MH electrolyser. The model consists of 3 sub-models: SOEC sub-model, MH sub-model and CFD sub-model coupled by the reaction mass sources of species and reaction heat sources as illustrated in Fig. 4. Finite Element Method is used to numerically solve this multi-physics problem in commercial software package COMSOL 4.0.

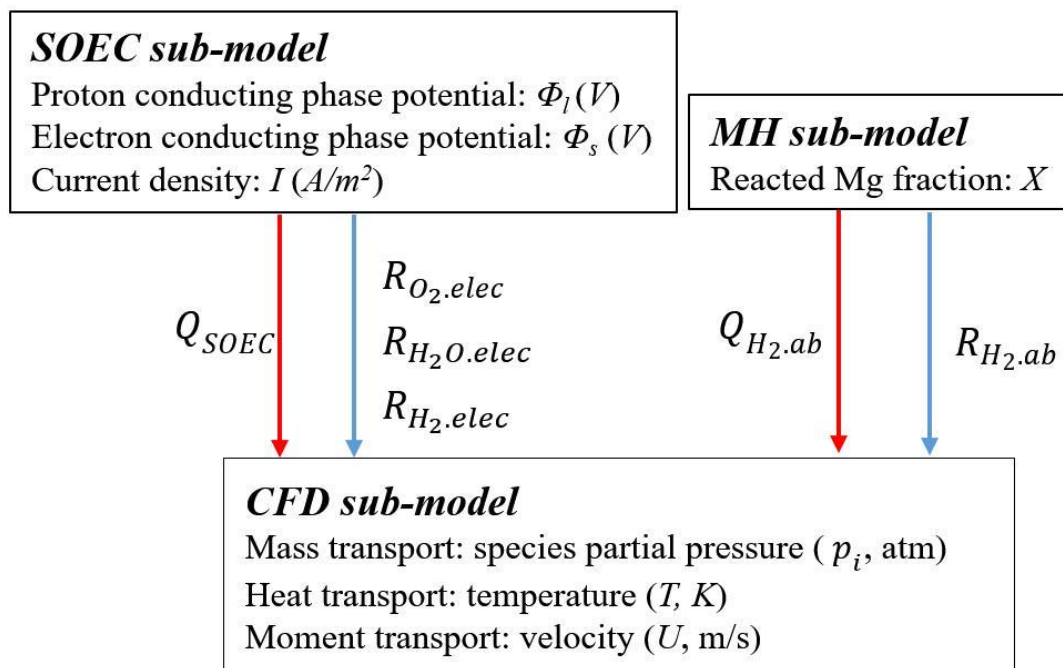


**Fig. 4** The implementation of sub-models by electrolysis heat source ( $Q_{SOEC}$ ), adsorption heat source ( $Q_{H_2.ab}$ ) and species sources of hydrogen ( $R_{H_2.ab}$ ,  $R_{H_2.elec}$ ), oxygen ( $R_{O_2.elec}$ ) and steam ( $R_{H_2O.elec}$ ).

## 4.1 SOEC sub-model

The SOEC model is used to calculate the reaction rates of steam electrolysis at given voltage. The two half reactions on air electrode side and fuel electrode are described by Eq. 1~2. The influence of pressure and temperature on the electrochemical reaction are considered in the Nernst equation and kinetic Butler-Volmer equation to calculate the equilibrium potential and activation overpotentials:

$$\text{Nernst equation: } E_{H_2O} = 1.253 - 0.00024516T + \frac{RT}{2F} \ln \left[ \frac{p_{H_2}(p_{O_2})^{0.5}}{p_{H_2O}^I} \right] \quad (4)$$

Butler-Volmer equations:

$$i_{source.c} = AV_c \cdot i_{o.c} \left( \exp \left( \frac{2F \cdot \eta_{act.c}}{RT} \right) - \frac{p_{H_2}}{p_{H_2.ref}} \exp \left( \frac{-2F \cdot \eta_{act.c}}{RT} \right) \right) \quad (5)$$

$$i_{source.a} = AV_a \cdot i_{o.a} \left( \frac{p_{H_2O}}{p_{H_2O.ref}} \exp \left( \frac{2F \cdot \eta_{act.a}}{RT} \right) - \frac{p_{O_2}}{p_{O_2.ref}} \exp \left( \frac{-2F \cdot \eta_{act.a}}{RT} \right) \right) \quad (6)$$

, where the  $i_o$  value are set as 4000 (A/m<sup>2</sup>) for cathode, 1300 (A/m<sup>2</sup>) for the anode [25].

The  $AV$  value are calibrated by experimental work [26] as  $2.33 \times 10^5$  (1/m) and  $2.46 \times 10^5$  (1/m) for cathode and anode, respectively.

The electrochemical reaction sources  $R_{i.elec}$  (kg/(m<sup>3</sup>·s)) of H<sub>2</sub>O, O<sub>2</sub> or H<sub>2</sub> could be calculated by  $i_{source}$ :

$$R_{i.elec} = \frac{v_i i_{source}}{nF} \quad (7)$$

The potential equilibrium at triple phase boundary (TPB) of electron conducting phase potential ( $\phi_s$  for SSC/Ni) and proton conducting phase ( $\phi_l$  for electrolyte material, BZCY) should be governed by the following equation:

$$\phi_l - \phi_s = E_{H_2O} - \eta_{act} \quad (8)$$

Equation. 6 together with the Ohm law (Eq. 7&8) will govern the charge conservation.

$$\mathbf{i}_l = -\sigma_{l.eff} \nabla(\phi_l), \quad \nabla \mathbf{i}_l = Q_l + i_{source} \quad (9)$$

$$\mathbf{i}_s = -\sigma_{s.eff} \nabla(\phi_s), \quad \nabla \mathbf{i}_s = Q_s - i_{source} \quad (10)$$

The local heat source in SOEC is calculated as  $Q_{SOEC}$ :

$$Q_{SOEC} = \sigma_{s/leff} \cdot i^2 + |\eta_{act}| \cdot i \quad (11)$$

For the properties parameters of the electrodes and electrolyte materials, readers can refer to Table. 2. Porosity ( $\varepsilon=0.55$ ) and tortuosity ( $\tau=2.5$ ) of the porous air electrode and fuel electrode are used to correct the effective electrical conductivities [27]. The volume fraction of Ni phase and SSC phase are both set as 0.28. More details regarding the SOEC electrochemical model follow the authors' previous work [28].

Table. 2 Physical properties of the SOEC materials.

SOEC section parameters	Thermal conductivity ( $\text{W}\cdot\text{m}^{-1}\cdot\text{K}^{-1}$ )	Density ( $\text{kg}\cdot\text{m}^{-3}$ )	Specific heat capacity ( $\text{J}\cdot\text{kg}^{-1}\cdot\text{K}^{-1}$ )	Electrical conductivity ( $\text{S}\cdot\text{m}^{-1}$ )
Ni [29]	71.8	8900	518	$\sigma_{Ni} = \frac{9.5 \cdot 10^7}{T} \cdot \exp\left(\frac{-1150}{T}\right)$
BZCY [30-32]	1.3	6200	407	$\sigma_{BZCY} = 290.4 \cdot \exp\left(\frac{-4600.6}{T}\right)$
SSC[33, 34]	0.6	7500	1960	$\sigma_{SSC} = 100 \cdot 10^{\left(2.12 + \frac{1183}{T} - \frac{4.38 \cdot 10^5}{T^2} + \frac{6 \cdot 10^7}{T^3}\right)}$

## 4.2 MH sub-model

The Mg/MgH<sub>2</sub> bed model is developed to calculate the kinetic H<sub>2</sub> absorption rate ( $R_{H_2,ab}$ ), heat source of the hydrogen adsorption ( $Q_{H_2,ab}$ ) of Eq. 3, and the reaction fraction of Mg ( $X$ ). The kinetic model is based on experimental testing and well validated numerical simulations from Chaise et al [35, 36] and Zewei et al [37] as follows:

$$R_{H_2,ab} = \rho_{MH} \cdot wt \cdot (1 - \varepsilon_{MH}) \cdot k_a \cdot e^{\frac{-E_a}{RT}} \cdot \frac{(p_{H_2} - p_{eq})}{p_{eq}} \cdot \frac{(1-X)^{2/3}}{1-(1-X)^{1/3}} \quad (12)$$

, where the gravimetric hydrogen storage capacity ( $w_t$ ) of Mg/MgH<sub>2</sub> bed is 6%. The  $\varepsilon_{MH}$  represents the porosity of Mg bed and  $\rho_{MH}$  as density the of pure Mg solid. The equilibrium pressure  $p_{eq}$  is determined by Van't Hoff equation:

$$\ln \frac{p_{eq}}{p_{ref}} = \frac{\Delta H}{RT_s} - \frac{\Delta S}{R} \quad (13)$$

Where the  $\Delta H = -75000$  J/(mol) and  $\Delta S = 135.6$  J/(mol·K) are the enthalpy change and entropy change of reaction Eq. 3 at standard condition. The reference pressure  $p_{ref}$  is set as 1 atm.

Knowing  $R_{H_2.ab}$ , the change rate of reacted Mg fraction ( $dX/dt$ ) can be expressed as:

$$\frac{dX}{dt} = \frac{R_{H_2.ab}}{\rho_{MH} \cdot w_t \cdot (1 - \varepsilon_{MH})} \quad (14)$$

Similarly, the heat source released by the H<sub>2</sub> absorption reaction:

$$Q_{H_2.ab} = \frac{(\Delta H + T_s(c_{p,g} - c_{p,MH}))}{M} \cdot R_{H_2.ab} \quad (15)$$

$T_s$  represents the temperature of solid Mg/MgH<sub>2</sub> bed;  $M$  is the molecular weight of Magnesium;  $C_{p,g}$  and  $C_{p,MH}$  are the specific heat of the fuel gas and Mg/MgH<sub>2</sub> bed, respectively. Table. 3 gives the MH section properties parameters used in the sub-model [36].

Table. 3 MH section properties

MH section model parameters [36]	Value
Maximum mass content of H of Mg hydride, $w_t$	6%
Density of Magnesium hydride powder, $\rho_{MH}$	1800 kg·m <sup>-3</sup>
Effective thermal conductivity of Magnesium powder, $\lambda_{s,MH}$	0.48 W·m <sup>-1</sup> ·K <sup>-1</sup>
Specific heat capacity of Magnesium hydride powder, $c_{p,MH}$	1545 J·kg <sup>-1</sup> ·K <sup>-1</sup>
Reaction rate constant, $k_a$	1·10 <sup>10</sup> s <sup>-1</sup>
Activation Energy, $E_a$	130 kJ
Porosity, $\varepsilon_{MH}$	0.74
Permeability, $\kappa_{MH}$	5.75·10 <sup>-14</sup> m <sup>2</sup>

### 4.3 CFD sub-model

The CFD sub-model consists of four kinds of governing equations: heat transport (Eq. 16 ~ 19), momentum transport (Eq. 20 ~ 21), species transport (Eq. 22 ~ 23) and mass transport (Eq. 24), following previous established CFD model for SOEC application [28]. The reaction sources and heat sources from SOEC sub-model and MH sub-model will influence the flow and heat transport in a coupled manner, thus to be introduced as sources terms into the three governing equations.

Heat transport for porous domains:

$$(\rho c_p)_{eff} \frac{\partial T}{\partial t} + \rho c_{p,g} U \cdot \nabla T + \nabla(-\lambda_{eff} \nabla T) = Q_{heat}; (Q_{SOEC} \text{ or } Q_{H_2.ab}) \quad (16)$$

, where the effective  $(\rho c_p)_{eff}$  should be express as the average of the solid phase and void phase:

$$(\rho c_p)_{eff} = \varepsilon \rho_g c_{p,g} + (1 - \varepsilon) \rho_s c_{p,s} \quad (17)$$

Similarly for thermal conductivity:

$$\lambda_{eff} = \varepsilon \lambda_g + (1 - \varepsilon) \lambda_s \quad (18)$$

In flow channel domains, the heat transport equation will change to:

$$(\rho_g c_{p,g}) \frac{\partial T}{\partial t} + \rho c_{p,g} U \cdot \nabla T + \nabla(-\lambda_g \nabla T) = 0 \quad (19)$$

Momentum transport for flow channel domains:

$$\rho_g \frac{\partial U}{\partial t} + \rho_g ((U \cdot \nabla) U) = \nabla \cdot \left[ -p + \mu(\nabla U + (\nabla U)^T) - \frac{2}{3} \mu(\nabla \cdot U) \right] \quad (20)$$

Momentum transport for porous domains:

$$\rho_g \frac{\partial U}{\partial t} + \frac{\rho_g}{\varepsilon} \left( (U \cdot \nabla) \frac{U}{\varepsilon} \right) = \nabla \cdot \left[ -p + \frac{\mu(\nabla U + (\nabla U)^T)}{\varepsilon} - \frac{2}{3} \frac{\mu}{\varepsilon} (\nabla \cdot U) \right] - \left( \mu \kappa^{-1} + \nabla(\rho_g U) \right) U \quad (21)$$

Species transport:

$$\rho_g \frac{\partial w_i}{\partial t} + \nabla \left( -\rho_g \cdot w_i \sum_{j \neq i}^n D_{ij} \nabla x_j + (x_j - w_j) \cdot \frac{\nabla p}{p} \cdot U \right) + \rho_g \cdot U \cdot \nabla w_j = 0 \quad (22)$$

$$\rho_g \frac{\partial w_i}{\partial t} + \nabla \left( -\rho_g \cdot w_i \sum_{j \neq i}^n D_{eff,ij} \nabla x_j + (x_j - w_j) \cdot \frac{\nabla p}{p} \cdot U \right) + \rho_g \cdot U \cdot \nabla w_j = R_{i.elec} \text{ or } R_{H_2.ab} \quad (23)$$

Mass transport:

$$\rho_g \frac{\partial \rho_g}{\partial t} + \nabla(\rho_g U) = R_{i.elec} \text{ or } R_{H_2.ab} \text{ or } 0 \quad (24)$$

Assumptions made in the CFD sub-model are summarized below:

- 1) The flow is incompressible viscous with Dusty Gas Model diffusion model.
- 2) Gas mixture properties are determined by the ideal gas law.
- 3) The local thermal equilibrium is assumed to be valid in both solid domain and porous domain.

#### 4.4 Boundary conditions and initial conditions

The two inlet conditions are both carefully tuning in order to keep the SOEC working at ca.900 ~ 950 K and the MH section at ca. 500 ~ 600 K. For the base case operating, the fuel inlet temperature is 1400 K, while the cooling air inlet is at 500 K as shown in Table. 1. The outer wall of the electrolyser's tube is set as heat insulation boundary.

For the initial conditions, the SOEC section is operated at 1.4 V with a current density of 4301 A/m<sup>2</sup>. The reacted fraction  $X$  of MH section will be set at 0 at  $t = 0$  s, then start to adsorb H<sub>2</sub>. The simulation time is 3000 s with a minimum time step of 0.01s.

#### 4.5 Validation of the model

The validation of the SOEC sub-model is conducted based on experimental results[38] of a BZCY-based SOEC using the corresponding cell configuration and geometry. The current-voltage curves fit well in 600 °C~700 °C with the voltage applied increase from OCV to 1.6V (Fig. 5), indicating the validity of the model in the operating range of the SOEC section.

The kinetics expression and thermochemical properties of MH sub-model are correlated from Chaise et al' s testing results of MH bed's adsorption process with good agreement as reported [35].

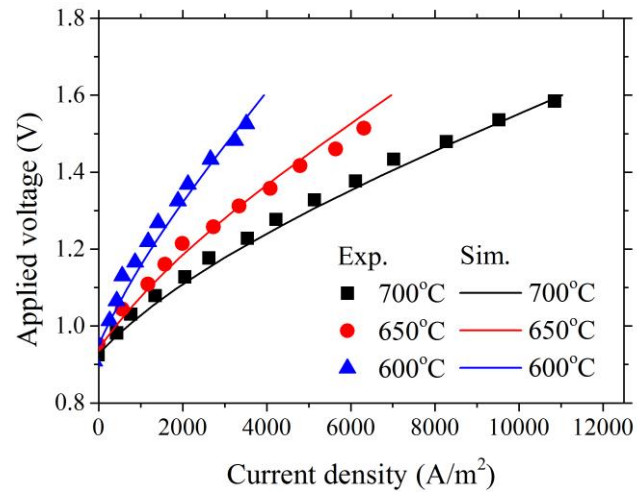


Fig. 5 SOEC sub-model validated with experimental results

## 5 Results & Discussion

The dynamic simulation of the base case study is conducted at conditions referred to Table.1, and followed by a series of sensitivity study on three important operating parameters: the electrolysis voltage ( $V_{op}$ ), operating pressure ( $p_{op}$ ), and inlet temperature of the cooling air ( $T_{airin}$ ). In this section, the simulated evolutions of temperature, reacted Mg fraction ( $X$ ), hydrogen partial pressure ( $p_{H_2}$ ) of the base case will firstly be analysed. Afterwards, the sensitivity of operating parameters would be discussed to provide optimization guidelines for design and operating strategy.

### 5.1 Base case simulation

Figure. 6 gives the transient 3D distribution of the tubular electrolyser in terms of  $p_{H_2}$ ,  $T$ , and  $X$  at  $t = 50$  s of the base case operating. It can be found that the  $p_{H_2}$  will

be increased from 2.0 atm to 2.1 atm when the flow pass by the SOEC section due to water electrolysis. Then  $p_{H_2}$  will be kept constant till the flow pass through the MH section, where, the hydrogen will diffuse into the porous MH bed, while being adsorbed by Mg. Therefore, the  $p_{H_2}$  inside the cylinder-shaped MH bed would be lower than that of periphery flow region, and distributed decreasingly from the centric axis ( $r = 0$ ) to the outer surface ( $r = r_{MH}$ ) due to the difficulty of  $H_2$  molecules diffusion. In the fuel flow direction, the  $p_{H_2}$  is also getting lower, hence the minimum  $p_{H_2}$  is found at the central point within the end surface of the MH bed as a value of 1.72 atm. For the temperature distribution from Fig. 6b, it generally decreases in the z direction as expected to help maintain SOEC section and MH section in good functioning temperature range as required. Notably, a subtle temperature enhancement in the MH section can be observed in the large temperature scale (500 ~ 1400 K). This increase is caused by the heat release from the hydrogen adsorption process. Fig. 6c is the  $X$  distribution of the MH bed at  $t = 50$  s with proper zoomed-in. The  $X$  value decreases when the flow permeates from the outside to the centric axis ( $r$  decreases) which is in accordance with the  $p_{H_2}$  distribution. However its distribution along the z-axis plausibly conflicts with the  $p_{H_2}$  distribution, which can be explained by the kinetic expression of the adsorption rate: at  $t = 50$  s, the adsorption rate is more determined by the equilibrium pressure  $p_{eq}$ , as expressed in Eq. 13 that the  $p_{eq}$  will decrease when the temperature decreases. The adsorption rate will accordingly increase when the  $p_{eq}$  decreases as described in Eq. 12 in case of adsorption ( $p > p_{eq}$ ).

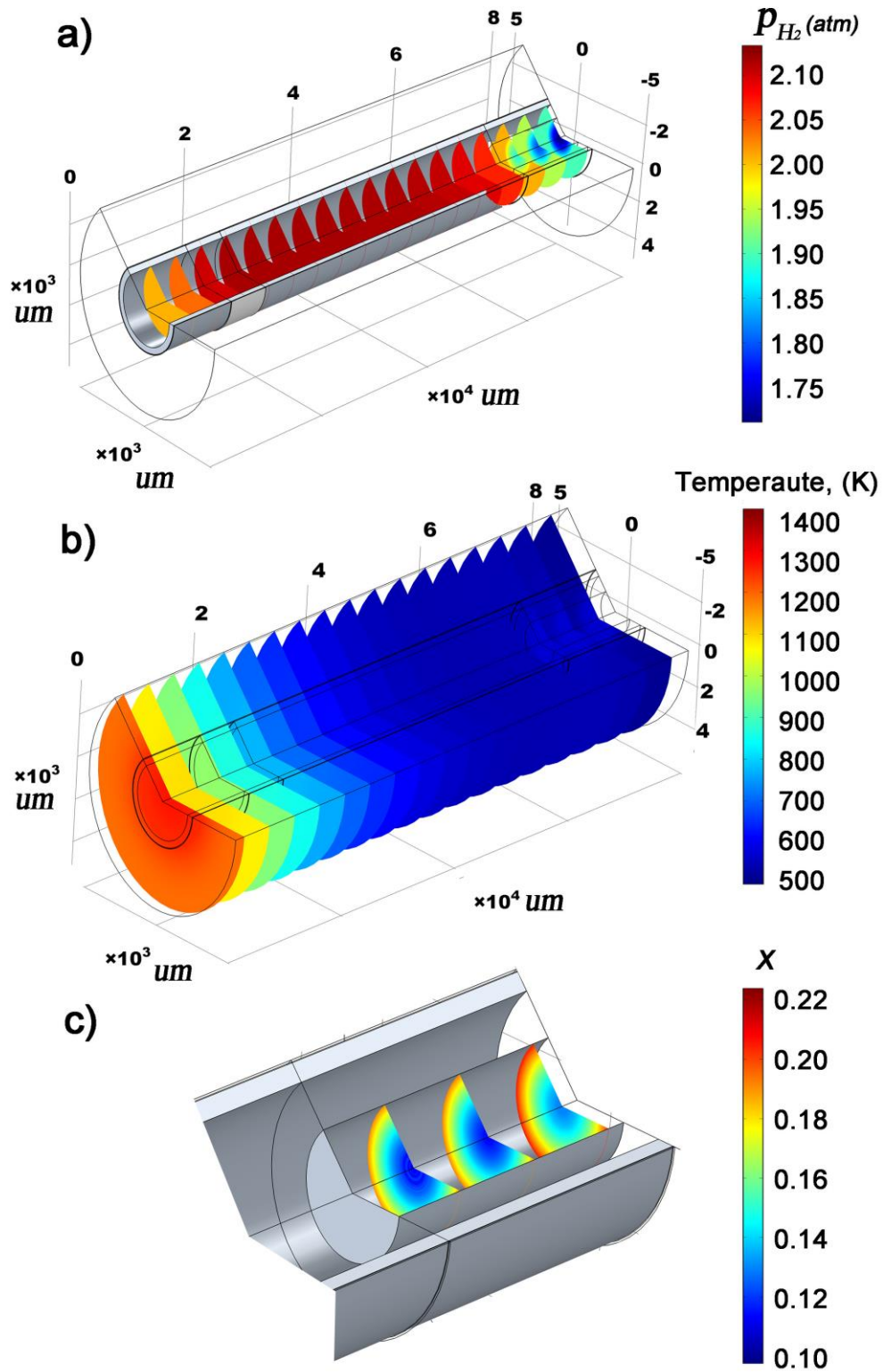


Fig. 6 Base case simulated results at  $t = 50$  s: a)  $H_2$  partial pressure distribution; b) temperature distribution; c) reacted Mg fraction distribution.

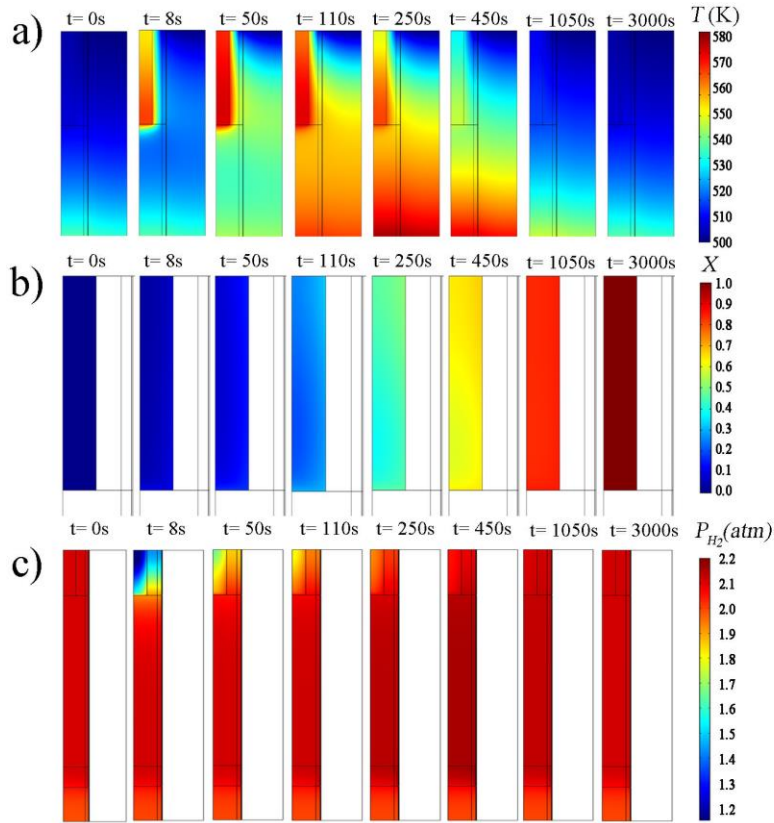


Fig. 7 Evolution of (a) temperature, (b) reacted Mg fraction, and (c)  $H_2$  partial pressure from 0 s to 3000 s of the base case.

Figure.7 shows the evolution of  $T$  and  $X$  in the  $z - r$  cut-plane of MH section, and the  $P_{H_2}$  in the whole computation domain. The temperature distribution verify the subtle temperature enhancement observed from Fig. 6b that: the heat generation due to hydrogen adsorption results in the heating up of MH bed for ca. 80 K (Maximum value at  $t = \text{ca. } 50 \text{ s}$ ) compared to the initial state. Besides, the contour flow configuration will help heat flux propagates to the down steam direction of the cooling air. This heat flux is believed to subsequently enhance the performance of SOEC section, which will further release more ohm heat dissipated from electrolysis reaction.

When the simulation process to 250 s, it can be found from Fig.7a that the flow temperature at the upstream of the fuel flow (between the SOEC section and MH

section) will be as high as 580 K. This can be considered as a response to the enhanced electrolysis current density.

The evolution of the reacted fraction ( $X$ ) in Fig. 7b shows that the adsorption capacity of the MH bed can be fulfilled before the end of the simulation ( $t = 3000$  s). It can also be inferred that the ending part of the cylinder bed reaches the fully charged state earlier than front part, and the outer part earlier than the inside part.

Figure. 7c shows the evolution of hydrogen partial pressure, indicating that the absorption rate is the fastest at the very start of the simulation according to the low value of  $p_{H_2}$  observed at ( $t = 8$  s).

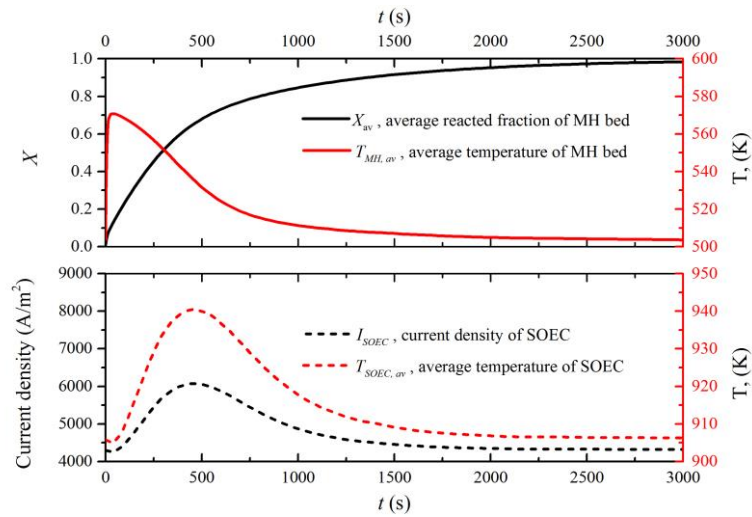


Fig. 8. The average  $X$  and temperature of the MH bed vs. time (up); the average temperature and current density of SOEC vs. time (down).

To clarify the enhancement effect of the absorption heat on the SOEC section, Fig. 8 shows the average temperature evolution of both the MH bed and SOEC anode layer. It is clearly shown that the peak value of  $T_{MH,av}$  occurs at  $t = \text{ca.}40$  s with a temperature rise of 65K, much earlier than that of the  $T_{SOEC,av}$  which occurs at  $t = \text{ca.}450$  s with a

smaller temperature rise of 35K. This lagging of temperature rise is due to the slow heat transport as the counter flow configuration stabilizes the temperature distribution.

As a result of the temperature enhancement, electrolysis current density ( $T_{SOEC,av}$ ) gains an increase of 1500 A/m<sup>2</sup> at  $t = \text{ca. } 450 \text{ s}$ , compared to the initial 4301 A/m<sup>2</sup>, and then converges to the initial value when the average  $X$  approaches 1.0.

Looking at the  $X_{av}$  curve of the base case in Fig. 8a, it takes 1950s to reaches 0.95. To better compare the absorption kinetics among different cases later,  $X_c=0.95$  is defined as the cut-off fraction, after which the MH bed is considered fully charged. The time consumed at  $X_c$  is defined as the cut-off time ( $t_c$ ).

The performance summary of the whole storage process is shown in Table. 4. It is worth noting that the amount of H<sub>2</sub> storage in MH bed is 55.9% of the hydrogen generated from electrolysis, defined as the H<sub>2</sub> storage efficiency ( $\eta_{H_2}$ ). Besides, the utilization rate of H<sub>2</sub>O is also very low (23.7%). Additional fuel/air flow container is suggested to be used in practical system design, to circulate the unabsorbed H<sub>2</sub> and unelectrolysed H<sub>2</sub>O so as to improve  $\eta_{H_2}$  and the H<sub>2</sub>O utilization rate in the system level.

Table. 4 Performance summary of the base case

Operating conditions	MH section		SOEC section	
	$p_{op} = 4 \text{ atm}$ $V_{op} = 1.4 \text{ V}$ $T_{airin} = 500 \text{ K}$ $T_{fuelin} = 1400 \text{ K}$	H <sub>2</sub> storage amount (at $t_c$ )	$7.35 \times 10^{-2} \text{ g}$	Average Current density (0 s~ $t_c$ )
Absorption time ( $t_c$ at $X_c=95\%$ )		1950 s	H <sub>2</sub> production rate	$4.05 \times 10^{-6} \text{ g/s}$
H <sub>2</sub> storage efficiency ( $\eta_{H_2}$ )		55.9%	H <sub>2</sub> O utilization rate	23.7%

Next, the effects of operating pressure, voltage and cooling air inlet temperature will be discussed by three sensitivity studies. In each study, only the parameter to be studied will be changed in a reasonable range, while keeping others the same with the base case.

Detailed simulation condition and results are summarized in Table. 5.

Table. 5 Summary of sensitivity studies on pressure, voltage and cooling air inlet temperature

Unvaried operative parameters	Varied operative parameter	Absorption time, $t_c$ (s)	Storage efficiency (%)	Electrolysis average current till $t_c$ , ( $A/m^2$ )
$V_{op} = 1.4$ V $T_{airin} = 500$ K	$P_{op} = 3$ atm	2790	38%	5049.86
	$P_{op} = 4$ atm	1950	56%	4956.40
	$P_{op} = 5$ atm	1426	76%	4960.41
	$P_{op} = 6$ atm	1109	97%	4994.59
$P_{op} = 4$ atm $T_{airin} = 500$ K	$V_{op} = 1.2$ V	2068	176%	1486.12
	$V_{op} = 1.3$ V	1987	98%	2769.47
	$V_{op} = 1.4$ V	1950	56%	4956.40
	$V_{op} = 1.5$ V	1649	22%	15043.24
$P_{op} = 4$ atm $V_{op} = 1.4$ V	$T_{airin} = 400$ K	>3000	50% ( $X = 0.477, t = 3000$ s)	1808.70 ( $t = 3000$ s)
	$T_{airin} = 450$ K	>3000	52% ( $X = 0.829, t = 3000$ s)	3008.83 ( $t = 3000$ s)
	$T_{airin} = 500$ K	1950	56%	4956.40
	$T_{airin} = 550$ K	2670	31%	6539.38

## 5.2 Effects of pressure

The performance of the electrolyzer is sensitive to the operating pressure, not only because of the pressure effect on the SOEC Nernst potential but also on MH bed's adsorption kinetics. Fig. 6 shows that the  $X$  value will increase with a faster rate when

increasing operating pressure ( $p_{op}$ ) from 3 atm to 6 atm. At the same time, the  $t_c$  value decreases from 2790s to 1110s (Table. 5). This can be simply explained by the increased initial  $p_{H_2}$ , which is proportional to  $p_{op}$ , enhancing the adsorption rate to a great extent.

On the other hand, when  $p_{op}$  increases, the SOEC current density can be reduced by 13% at the initial state, since the Nernst potential ( $E_{H_2O}$ ) are getting higher, which overwhelms the benefits getting from the reduction of activation overpotential at higher  $p_{op}$ . However, the average current densities ( $I_{SOEC,av}$ ) throughout the whole adsorption process bound by  $t = 0$  s and  $t = t_c$  s, are almost the same at different  $p_{op}$  according to the summarized results in Table. 5. This is because the current density goes up more quickly in cases of higher pressure, approaching maximum current densities nearly of the same value as observed from Fig. 9. That is to say, when operating at high current density, the negative effects of increasing pressure on SOEC's Nernst potential are balanced out by its positive effect on the activation overpotential as shown in Eq. 5~6.

For the storage efficiency, it is also largely improved from 38.3% to 97%, mainly due to the shortening of  $t_c$ . By doing this sensitivity study, it can be concluded that it is beneficial to increase the operating pressure in terms of theoretical storage efficiency and adsorption period.

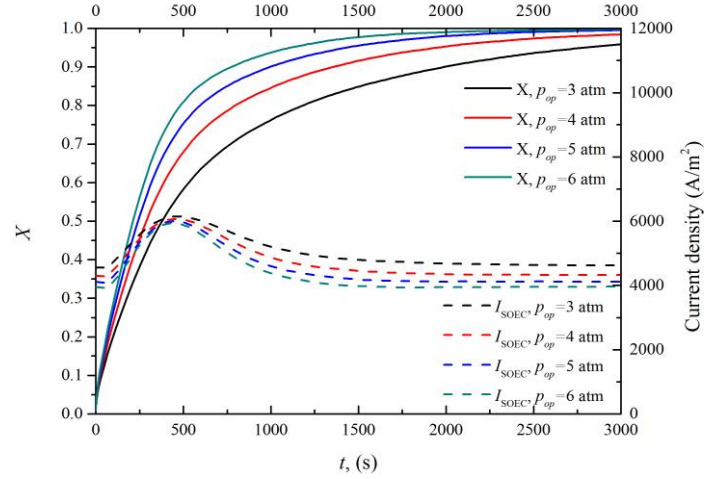


Fig. 9. Evolution of  $X$  and current density of SOEC section ( $I_{SOEC}$ ) vs. time at different operating pressure.

### 5.3 Effects of operating voltage

When the operating voltage ( $V_{op}$ ) is increased from 1.2 V to 1.5 V, the current density is dramatically improved just as expected in Fig. 10, indicating that  $H_2$  generation is proportionally boosted, whereas the  $H_2$  storage is not as much as enhanced: the  $t_c$  value is only reduced by 20.26%, leading to a rapid decline of storage efficiency to 22% at 1.5 V as shown in Table. 5. Apparently in high voltage cases, there would be large amount of  $H_2$  cannot be absorbed before exhausting out of the MH bed. On the country, it should be noted that the high storage efficiency at 1.2 V is 176%, larger than 100% since the MH bed absorbs all the  $H_2$  generated from electrolysis, plus an amount of  $H_2$  originally from the carrier gas (76% of  $H_2$  generated by electrolysis).

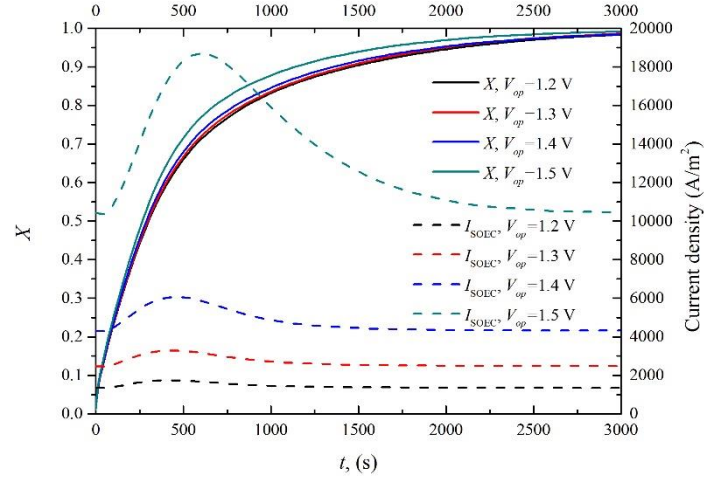


Fig. 10. Evolution of  $X$  and current density of SOEC section ( $I_{SOEC}$ ) vs. time at different operating voltage ( $V_{op}$ ).

From the viewpoint of continuous operation, the existing of the carrier gas can empower the electrolyser the ability to shift peak load to some extent if well recirculated: When the electricity load is high, redundant  $H_2$  will be generated, resulting in high  $H_2$  partial pressure exhausting the electrolyser, and then the  $H_2$  enriched flow being recirculated back to the fuel inlet with sufficient heat recuperating. The excessive  $H_2$  is kind of temporarily stored in the fuel flow pipes other than the MH bed in peak load situations. When the electricity load goes down, the previously stored  $H_2$  in pipes can be used to compensate the low  $H_2$  generation rate at low current operation, showing a storage efficiency bigger than 100% for the time being. By doing so, a relatively stable rate of  $H_2$  adsorption can be achieved through the whole peak-valley load period, as the  $t_c$  value does not changed much when changing the operating voltage.

#### 5.4 Effects of cooling air temperature

The air flow temperature is playing a key role in maintaining the electrolyzer in the desired temperature distribution, thus need to be carefully studied. When increasing the  $T_{airin}$  from 400 K to 550 K, we can find that the initial current density of SOEC

monotonously improved from 1713.5 A/m<sup>2</sup> to 6738.4 A/m<sup>2</sup> in Fig. 11, as the working temperature of SOEC will rises due to the weaken cooling effect from air flow. The  $X$  curves, however, shows the different trend that it first decreases, from too sluggish ( $t_c$  larger than 3000 s) to  $t_c = 1950$ s at 500K, and then  $t_c$  tends to go larger when further increasing  $T_{airin}$  to 550 K. Please be noted that the corresponding storage efficiency (%) and average electrolysis current density as shown in Table. 5 is calculated at  $t = 3000$ s in cases that  $t_c$  is beyond the simulation time range.

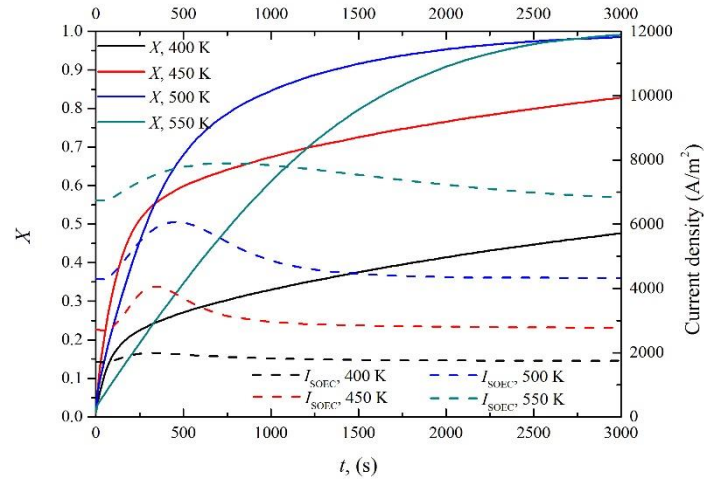


Fig. 11. Evolution of  $X$  and current density of SOEC section ( $I_{SOEC}$ ) vs. time at different air flow inlet temperature ( $T_{airin}$ ).

The reason for this tendency should be ascribed to the different limiting factors of  $dX/dt$  at different time according to Eq. 12. Firstly, when the  $X$  is close to 0, the adsorption reaction is limited by temperature since the  $H_2$  partial pressure is far from equilibrium state ( $p_{H_2}$  much larger than  $p_{eq}$ ), therefore cases with higher  $T_{airin}$  shows the higher slope of  $X$  curve (Fig. 11). When  $X$  gets higher, the  $(p_{H_2} - p_{eq})/p_{eq}$  term become the limiting factor, of which the  $p_{eq}$  is larger in high temperature cases, indicating that the  $dX/dt$  should be more suppressed because the  $(p_{H_2} - p_{eq})/p_{eq}$

tends to decrease faster when the  $X$  increases in high temperature cases, considering that  $p_{H_2}$  does not change much. Briefly speaking, the adsorption kinetic are limited by activation process ( $e^{\frac{-E_a}{RT}}$ ) at low  $T_{airin}$  cases, but limited by the Mg-MgH<sub>2</sub> equilibrium at high  $T_{airin}$  cases. This can be also verified in the phase equilibrium diagram (Fig. 3) that the slope of the normal line of the equilibrium curve, which is tangent to the equilibrium curve, denoting the best direction to improve absorption kinetics, would be more close to 0. Obviously, when the slope is close to 0, it is wiser to change the temperature, on the other hand when the slope is more negative, it is better to increase the partial pressure of H<sub>2</sub>.

An optimal  $T_{airin}$  value was found at 521 K with the optimal  $t_c$  as 1612 s, simply by conducting more parameter sweeping at smaller steps, of which the details are not included in this paper for concise reason.

## 6 Conclusions and Remarks

In this work, a novel electrolyser design is proposed for hydrogen generation and storage. Proton-conducting SOEC and metal hydride bed are integrated as two sections into one tubular electrolyser. The performance of the SOEC section and metal hydride section are dynamically simulated at pressurized conditions. An average current density of 4956.40 A/m<sup>2</sup> can be achieved when the MH section is 95% fully charged, yielding an H<sub>2</sub> storage efficiency of 56%.

Sensitivity studies are conducted to investigate the effects of operating pressure, operating voltage and cooling air inlet temperature. Simulated results indicate that it is wise to operate the electrolyzer at elevated pressure for shorter adsorption time and higher H<sub>2</sub> storage efficiency.

Secondly, increasing the operating voltage can reduce the adsorption time, but H<sub>2</sub> storage efficiency will be sacrificed. It is also found that the electrolyser owns the merits of shifting peak load by storing the excessive H<sub>2</sub> in the fuel pipe system if the fuel & air flow well recirculated in the case of volatile applied voltage.

Thirdly, there existing an optimal value of the cooling air inlet temperature, e.g. 510 K in the case of operating under 1.4 V and 4 atm, at which the adsorption time is shortest. While the H<sub>2</sub> storage efficiency would increase when the air inlet temperature decreases, as long as the  $t_c$  is within the maximum adsorption time as regulated (3000 s in this study).

Conclusions from the sensitivity study provide guidelines for designing the operating condition of the novel electrolyser in practical situations where the adsorption time, H<sub>2</sub> storage efficiency or the load of electricity are specified by clients. But more research works are needed in the mechanic design of the electrolyser such as the mount & dismantle strategy of the MH section. The electrolyzer is also promising for reversible operation as a solid oxide flow battery if switching strategy between the SOEC-MH (adsorption) mode and SOFC-MH (desorption) mode can be addressed in further works.

### **Acknowledgement**

This research is supported by a grant of SFC/RGC Joint Research Scheme (X-PolyU/501/14) from Research Grant Council, University Grants Committee, Hong Kong SAR.

We gratefully acknowledge the financial support of the National Science Foundation of China (Grant No. 51406091 and Grant No. 21406095).

## 7 Nomenclature

### Abbreviation

BZCY	BaCe <sub>0.5</sub> Zr <sub>0.3</sub> Y <sub>0.2</sub> O <sub>3-δ</sub>
CFD	Computational fluid dynamics
CHP	Combined heat power system
CNF	Carbon nanofibers
CNT	Carbon nanotubes
HT-PEM	High temperature proton exchange membrane fuel cell
MH	Metal hydride bed
MOF	Metal organic framework
OCV	Open circuit voltage
PEM	Proton exchange membrane
SOEC	Solid oxide electrolysis cell
SSC	Sm <sub>0.5</sub> Sr <sub>0.5</sub> CoO <sub>3-δ</sub>
TPB	Triple phase boundary

### Letters

$AV_a, AV_c$	Electrochemically active specific surface area, m <sup>-1</sup>
$D_{eff,ij}$	Effective binary diffusion coefficient of $i$ and $j$ , m <sup>2</sup> ·s <sup>-1</sup>
$D_{ij}$	Binary diffusion coefficient of species $i$ and $j$ , m <sup>2</sup> ·s <sup>-1</sup>
$E_{H_2O}$	Equilibrium Nernst potential of H <sub>2</sub> O electrolysis, V
$E_a$	Activation energy, J·mol <sup>-1</sup>
$I_{SOEC}$	Current density of SOEC, A·m <sup>-2</sup>
$L_{MH}$	Length of the MH bed, mm
$L_{SOEC}$	Length of the SOEC section (cathode layer coated), mm
$Q_{H_2,ab}$	Heat source due to hydrogen adsorption, J·m <sup>-3</sup> ·s <sup>-1</sup>
$Q_{SOEC}$	Heat source due to electrolysis, J·m <sup>-3</sup> ·s <sup>-1</sup>
$R_{H_2,ab}$	Reaction rate of hydrogen absorption in MH bed, kg·m <sup>-3</sup> ·s <sup>-1</sup>
$R_{i,elec}$	Reaction rate of species due to electrolysis, kg·m <sup>-3</sup> ·s <sup>-1</sup>
$T_{MH,av}$	Average temperature of MH section, K
$T_{SOEC,av}$	Average temperature of SOEC section, K
$T_{airin}$	Inlet temperature of air flow, K
$T_{fuelin}$	Inlet temperature of fuel flow, K
$V_{op}$	Operating voltage, V
$c_p$	Specific heat, J·kg <sup>-1</sup> ·K <sup>-1</sup>
$i_{o.a/c}$	Exchange current density, A·m <sup>-2</sup>
$i_{source.a}$	Local current source of anode (air side), A·m <sup>-3</sup>
$i_{source.c}$	Local current source of cathode (fuel side), A·m <sup>-3</sup>
$k_a$	Reaction rate constant, 2.98×10 <sup>-8</sup> , s <sup>-1</sup>
$p_i$	partial Pressure of species $i$ , Pa

$r_E$	Outer radius of the SOEC-MH electrolyser's cooling air channel, mm
$r_{MH}$	Radius of the MH bed, mm
$r_{SOEC}$	Outer radius of the SOEC tube, mm
$v_i$	Stoichiometric number of species $i$
$w_i$	Mass fraction of species $i$
$w_t$	Gravimetric hydrogen storage capacity, %
$x_j$	Mole fraction of species $j$
$\eta_{H_2}$	H <sub>2</sub> storage efficiency
$\eta_{act}$	Activation polarization, V
$\eta_{ohmic}$	Ohmic polarization, V
$\Phi$	Potential, V
$\Delta H$	Enthalpy change
$\Delta S$	Entropy change
$t$	Time, s
$L$	Length of the SOEC-MH electrolyser, mm
$M$	Molecular weight of Magnesium, 24.3 g/mol
$R$	Gas constant, 8.314 J·mol <sup>-1</sup> ·K <sup>-1</sup>
$T$	Local temperature, K
$U$	Velocity field, m <sup>3</sup> ·s <sup>-1</sup>
$X$	Reacted fraction of Mg
$i$	Local current density, A·m <sup>-2</sup>
$p$	Pressure, Pa
$\varepsilon$	Porosity
$\kappa$	Permeability, m <sup>2</sup>
$\kappa$	Permeability, m <sup>2</sup>
$\lambda$	Thermal conductivity, W·m <sup>-1</sup> ·K <sup>-1</sup>
$\mu$	Dynamic viscosity of fluid, Pa·s
$\rho$	Density, kg·m <sup>-3</sup>
$\sigma$	Conductivity for ion/electron, s·m <sup>-1</sup>
$\tau$	Tortuosity factors

## Subscripts

a	Anode
ab	Absorption
act	Activation
airin	Air flow inlet
av	Average
c	Cathode or cutoff
eff	Effective
eq	Equilibrium
g	Gas phase
i	Species index
l	Electrolyte

op	Operating
ref	Reference
s	Solid

## Reference

- [1] Haryanto A, Fernando S, Murali N, Adhikari S. Current status of hydrogen production techniques by steam reforming of ethanol: a review. *Energ Fuel*. 2005;19:2098-106.
- [2] Grimes CA, Varghese OK, Ranjan S. *Hydrogen generation by water splitting*: Springer; 2008.
- [3] Zhang H, Lin G, Chen J. Evaluation and calculation on the efficiency of a water electrolysis system for hydrogen production. *International Journal of Hydrogen Energy*. 2010;35:10851-8.
- [4] Ni M, Leung MKH, Leung DYC, Sumathy K. A review and recent developments in photocatalytic water-splitting using for hydrogen production. *Renewable and Sustainable Energy Reviews*. 2007;11:401-25.
- [5] Turner JA. Sustainable hydrogen production. *Science*. 2004;305:972-4.
- [6] Pan Z, Liu Q, Zhang L, Zhang X, Chan SH. Study of Activation Effect of Anodic Current on  $\text{La}_{0.6}\text{Sr}_{0.4}\text{Co}_{0.2}\text{Fe}_{0.8}\text{O}_{3-\delta}$  Air Electrode in Solid Oxide Electrolyzer Cell. *Electrochimica Acta*. 2016;209:56-64.
- [7] Pan Z, Liu Q, Zhang L, Zhou J, Zhang C, Chan SH. Experimental and thermodynamic study on the performance of water electrolysis by solid oxide electrolyzer cells with Nb-doped Co-based perovskite anode. *Applied Energy*. 2017;191:559-67.
- [8] Brisse A, Schefold J, Zahid M. High temperature water electrolysis in solid oxide cells. *International Journal of Hydrogen Energy*. 2008;33:5375-82.
- [9] Ni M, Leung MKH, Leung DYC. Technological development of hydrogen production by solid oxide electrolyzer cell (SOEC). *International Journal of Hydrogen Energy*. 2008;33:2337-54.
- [10] Zheng J, Liu X, Xu P, Liu P, Zhao Y, Yang J. Development of high pressure gaseous hydrogen storage technologies. *International Journal of Hydrogen Energy*. 2012;37:1048-57.
- [11] Alekseev A. *Hydrogen Liquefaction*. *Hydrogen Science and Engineering : Materials, Processes, Systems and Technology*: Wiley-VCH Verlag GmbH & Co. KGaA; 2016. p. 733-62.
- [12] Züttel A, Hirscher M, Panella B, Yvon K, Orimo S-i, Bogdanović B, et al. *Hydrogen Storage. Hydrogen as a Future Energy Carrier*: Wiley-VCH Verlag GmbH & Co. KGaA; 2008. p. 165-263.
- [13] Li J, Furuta T, Goto H, Ohashi T, Fujiwara Y, Yip S. Theoretical evaluation of hydrogen storage capacity in pure carbon nanostructures. *The Journal of Chemical Physics*. 2003;119:2376-85.
- [14] Chambers A, Park C, Baker RTK, Rodriguez NM. Hydrogen Storage in Graphite Nanofibers. *The Journal of Physical Chemistry B*. 1998;102:4253-6.
- [15] Rosi NL, Eckert J, Eddaoudi M, Vodak DT, Kim J, O'Keeffe M, et al. Hydrogen Storage in Microporous Metal-Organic Frameworks. *Science*. 2003;300:1127-9.
- [16] Schlapbach L, Züttel A. Hydrogen-storage materials for mobile applications. *Nature*. 2001;414:353-8.
- [17] Førde T, Eriksen J, Pettersen AG, Vie PJS, Ulleberg Ø. Thermal integration of a metal hydride storage unit and a PEM fuel cell stack. *International Journal of Hydrogen Energy*. 2009;34:6730-9.
- [18] Rizzi P, Pinatel E, Luetto C, Florian P, Graizzaro A, Gagliano S, et al. Integration of a PEM fuel cell with a metal hydride tank for stationary applications. *Journal of Alloys and Compounds*. 2015;645, Supplement 1:S338-S42.
- [19] Delhomme B, Lanzini A, Ortigoza-Villalba GA, Nachev S, de Rango P, Santarelli M, et al. Coupling and thermal integration of a solid oxide fuel cell with a magnesium hydride tank. *International Journal of Hydrogen Energy*. 2013;38:4740-7.
- [20] Urbanczyk R, Peil S, Bathen D, Heßke C, Burfeind J, Hauschild K, et al. HT-PEM Fuel Cell System with Integrated Complex Metal Hydride Storage Tank. *Fuel Cells*. 2011;11:911-20.

- [21] Shiraki M, Yakabe H, Uchida H. Efficiency Calculations for SOFC/SOEC Reversible System and Evaluations of Performances of Button-Size Anode-Supported Cell. *Ecs Transactions*. 2013;57:3261-7.
- [22] Chen P, Akiba E, Orimo S-i, Zuttel A, Schlapbach L. Hydrogen Storage by Reversible Metal Hydride Formation. *Hydrogen Science and Engineering : Materials, Processes, Systems and Technology*: Wiley-VCH Verlag GmbH & Co. KGaA; 2016. p. 763-90.
- [23] de Rango P, Marty P, Fruchart D. Hydrogen storage systems based on magnesium hydride: from laboratory tests to fuel cell integration. *Applied Physics A*. 2016;122:126.
- [24] Chen L, Chen F, Xia C. Direct synthesis of methane from CO<sub>2</sub>-H<sub>2</sub>O co-electrolysis in tubular solid oxide electrolysis cells. *Energ Environ Sci*. 2014;7:4018-22.
- [25] Ni M, Leung MKH, Leung DYC. Electrochemical modeling of hydrogen production by proton-conducting solid oxide steam electrolyzer. *International Journal of Hydrogen Energy*. 2008;33:4040-7.
- [26] He F, Song D, Peng R, Meng G, Yang S. Electrode performance and analysis of reversible solid oxide fuel cells with proton conducting electrolyte of BaCe<sub>0.5</sub>Zr<sub>0.3</sub>Y<sub>0.2</sub>O<sub>3-δ</sub>. *Journal of Power Sources*. 2010;195:3359-64.
- [27] Cussler EL. *Diffusion: mass transfer in fluid systems*: Cambridge university press; 2009.
- [28] Chen B, Xu H, Ni M. Modelling of SOEC-FT reactor: Pressure effects on methanation process. *Applied Energy*. 2017;185, Part 1:814-24.
- [29] Petruzzi L, Cocchi S, Fineschi F. A global thermo-electrochemical model for SOFC systems design and engineering. *Journal of Power Sources*. 2003;118:96-107.
- [30] Chen D, Zhang Q, Lu L, Periasamy V, Tade MO, Shao Z. Multi scale and physics models for intermediate and low temperatures H<sup>+</sup>-solid oxide fuel cells with H<sup>+</sup>/e<sup>-</sup>/O<sub>2</sub><sup>-</sup> mixed conducting properties: Part A, generalized percolation theory for LSCF-SDC-BZCY 3-component cathodes. *Journal of Power Sources*. 2016;303:305-16.
- [31] Yamanaka S, Hamaguchi T, Oyama T, Matsuda T, Kobayashi S-i, Kurosaki K. Heat capacities and thermal conductivities of perovskite type BaZrO<sub>3</sub> and BaCeO<sub>3</sub>. *Journal of Alloys and Compounds*. 2003;359:1-4.
- [32] Zhong Z. Stability and conductivity study of the BaCe<sub>0.9-x</sub>Zr<sub>x</sub>Y<sub>0.1</sub>O<sub>2.95</sub> systems. *Solid State Ionics*. 2007;178:213-20.
- [33] Sathyamoorthy B, Md Gazzali PM, Murugesan C, Chandrasekaran G. Electrical properties of samarium cobaltite nanoparticles synthesized using Sol-Gel autocombustion route. *Materials Research Bulletin*. 2014;53:169-76.
- [34] Nagai T, Ito W, Sakon T. Relationship between cation substitution and stability of perovskite structure in SrCoO<sub>3-δ</sub>-based mixed conductors. *Solid State Ionics*. 2007;177:3433-44.
- [35] Chaise A, Marty P, Rango Pd, Fruchart D. A simple criterion for estimating the effect of pressure gradients during hydrogen absorption in a hydride reactor. *International Journal of Heat and Mass Transfer*. 2009;52:4564-72.
- [36] Chaise A, de Rango P, Marty P, Fruchart D. Experimental and numerical study of a magnesium hydride tank. *International Journal of Hydrogen Energy*. 2010;35:6311-22.
- [37] Bao Z. Performance investigation and optimization of metal hydride reactors for high temperature thermochemical heat storage. *International Journal of Hydrogen Energy*. 2015;40:5664-76.
- [38] He F, Wu T, Peng R, Xia C. Cathode reaction models and performance analysis of Sm<sub>0.5</sub>Sr<sub>0.5</sub>CoO<sub>3-δ</sub>-BaCe<sub>0.8</sub>Sm<sub>0.2</sub>O<sub>3-δ</sub> composite cathode for solid oxide fuel cells with proton conducting electrolyte. *Journal of Power Sources*. 2009;194:263-8.

## List of Figures

**Fig. 1** Pressure–concentration–temperature plot (left) and a Van't Hoff curve (right) for LaNi<sub>5</sub>. The vertical axes indicate the corresponding hydrogen pressure or the equivalent electrochemical potential [16].

**Fig. 2** Schematic of the tubular electrolyser with the SOEC section and MH section at base case operation (scaled for better display)

**Fig. 3** The H<sub>2</sub> pressure-temperature diagram of the phase equilibrium between Mg/MgH<sub>2</sub>. Reaction time is denoted with the grey color level [23].

**Fig. 4** The implementation of sub-models by electrolysis heat source ( $Q_{SOEC}$ ), adsorption heat source ( $Q_{H_2,ab}$ ) and species sources of hydrogen ( $R_{H_2,ab}$ ,  $R_{H_2,elec}$ ), oxygen ( $R_{O_2,elec}$ ) and steam ( $R_{H_2O,elec}$ ).

**Fig. 5** SOEC sub-model validated with experimental results

**Fig. 6** Base case simulated results at  $t = 50$  s: a) H<sub>2</sub> partial pressure distribution; b) temperature distribution; c) reacted Mg fraction distribution.

**Fig. 7** Evolution of (a) temperature, (b) reacted Mg fraction, and (c) H<sub>2</sub> partial pressure from 0 s to 3000 s of the base case.

**Fig. 8** The average  $X$  and temperature of the MH bed vs. time (up); the average temperature and current density of SOEC vs. time (down).

**Fig. 9** Evolution of  $X$  and current density of SOEC section ( $I_{SOEC}$ ) vs. time at different operating pressure.

**Fig. 10** Evolution of  $X$  and current density of SOEC section ( $I_{SOEC}$ ) vs. time at different operating voltage ( $V_{op}$ ).

**Fig. 11** Evolution of  $X$  and current density of SOEC section ( $I_{SOEC}$ ) vs. time at different air flow inlet temperature ( $T_{airin}$ ).

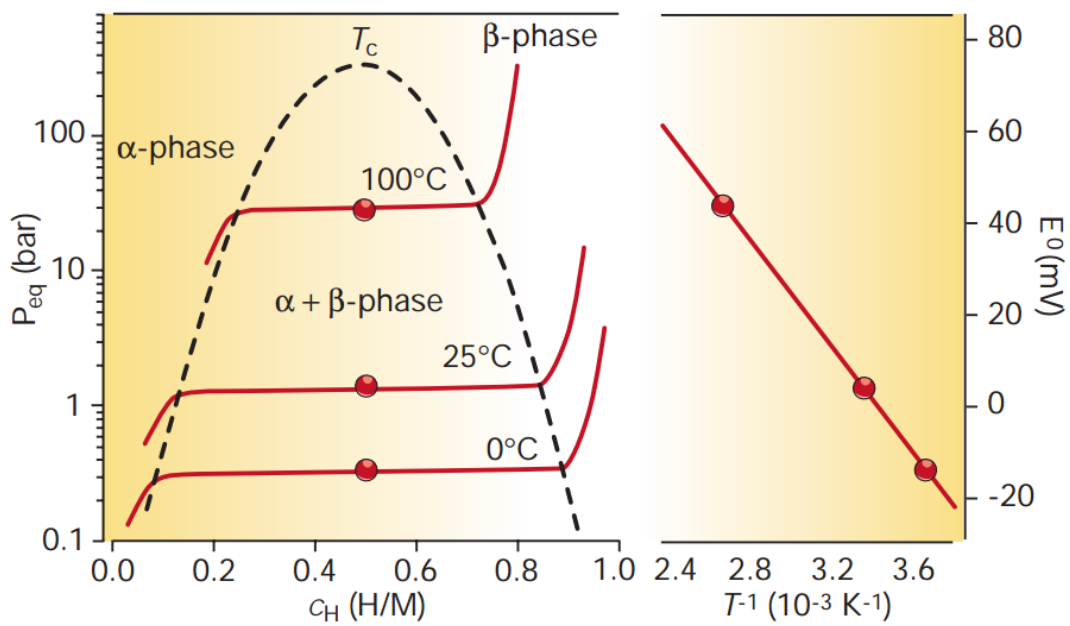


**Fig. 1** Pressure–concentration–temperature plot (left) and a Van't Hoff curve (right) for LaNi<sub>5</sub>. The vertical axes indicate the corresponding hydrogen pressure or the equivalent electrochemical potential [16].

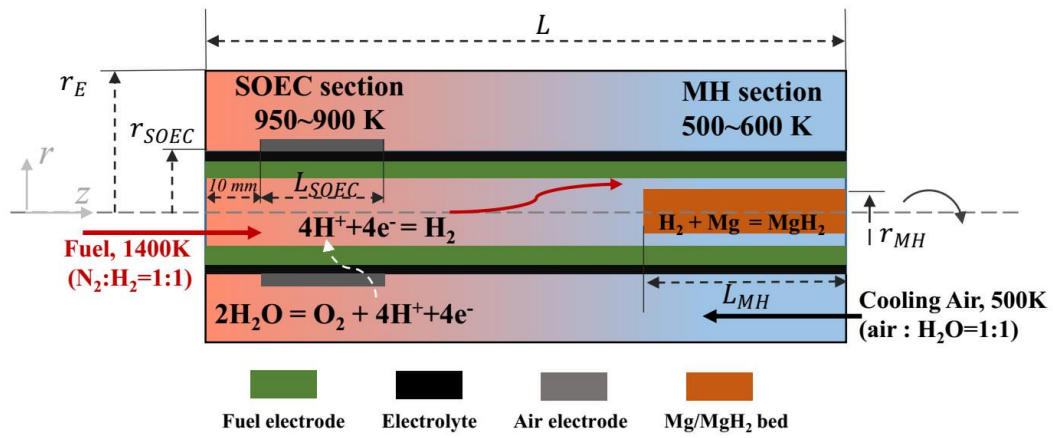


**Fig. 2** Schematic of the tubular electrolyser with the SOEC section and MH section at base case operation (scaled for better display)

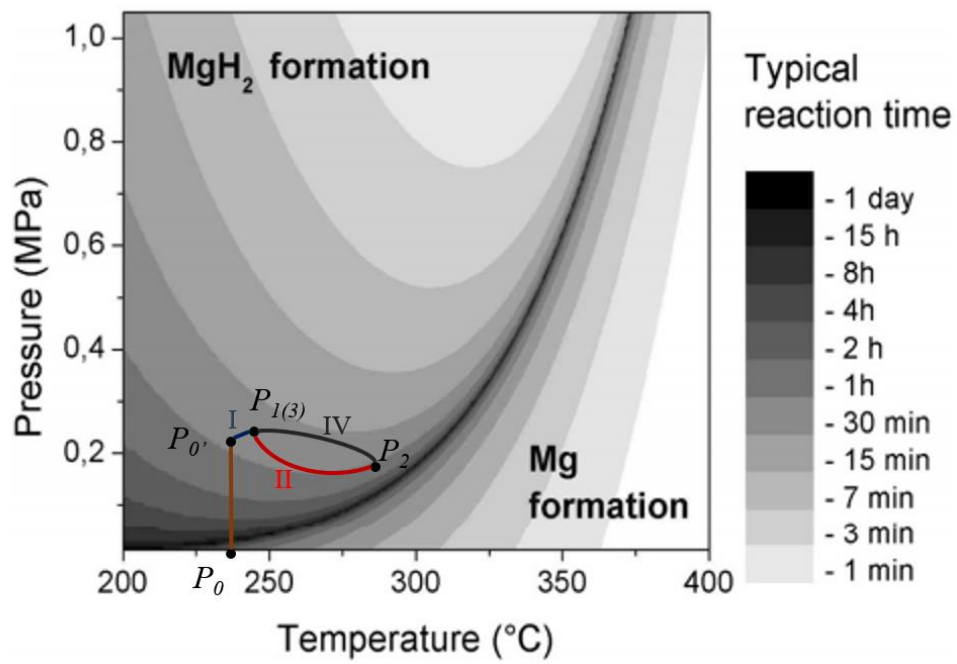


**Fig. 3** The H<sub>2</sub> pressure-temperature diagram of the phase equilibrium between Mg/MgH<sub>2</sub>. Reaction time is denoted with the grey color level [23].

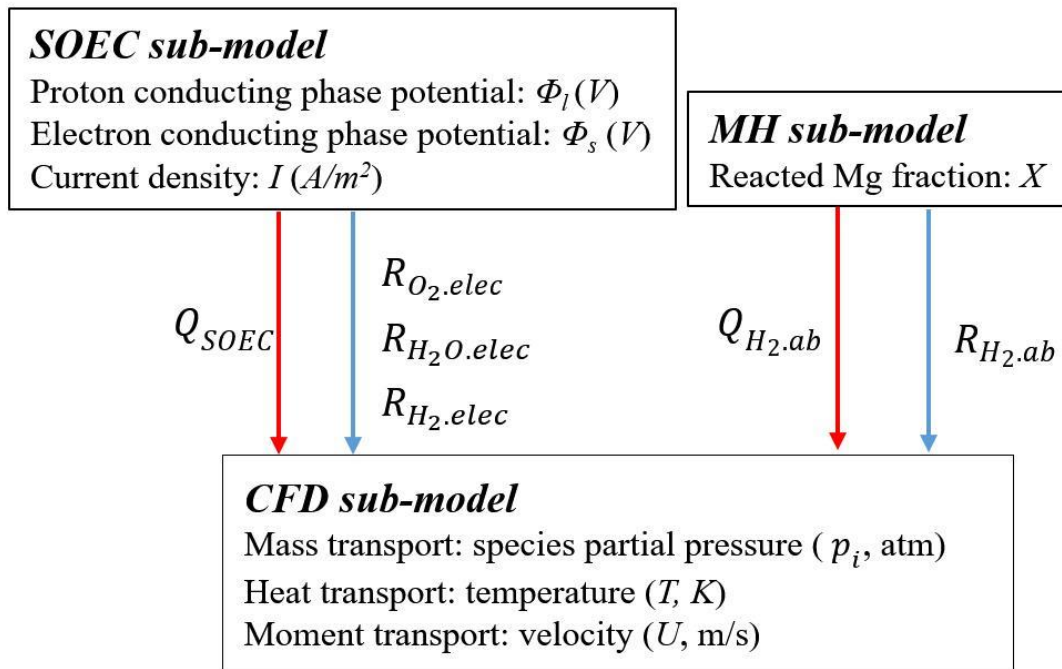


**Fig. 4** The implementation of sub-models by electrolysis heat source ( $Q_{SOEC}$ ), adsorption heat source ( $Q_{H_2.ab}$ ) and species sources of hydrogen ( $R_{H_2.ab}$ ,  $R_{H_2.elec}$ ), oxygen ( $R_{O_2.elec}$ ) and steam ( $R_{H_2O.elec}$ ).

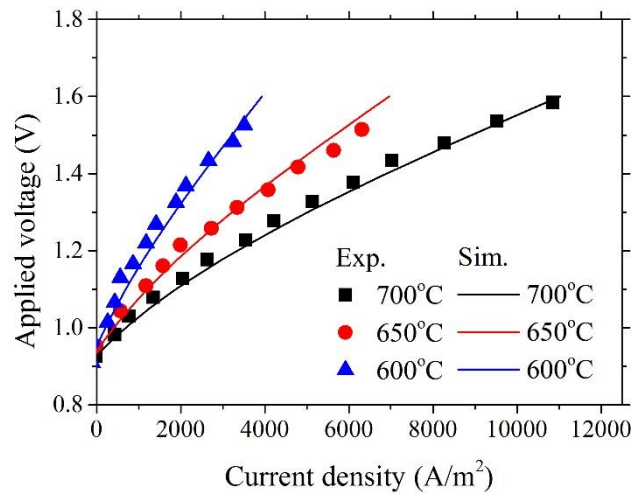


**Fig. 5** SOEC sub-model validated with experimental results

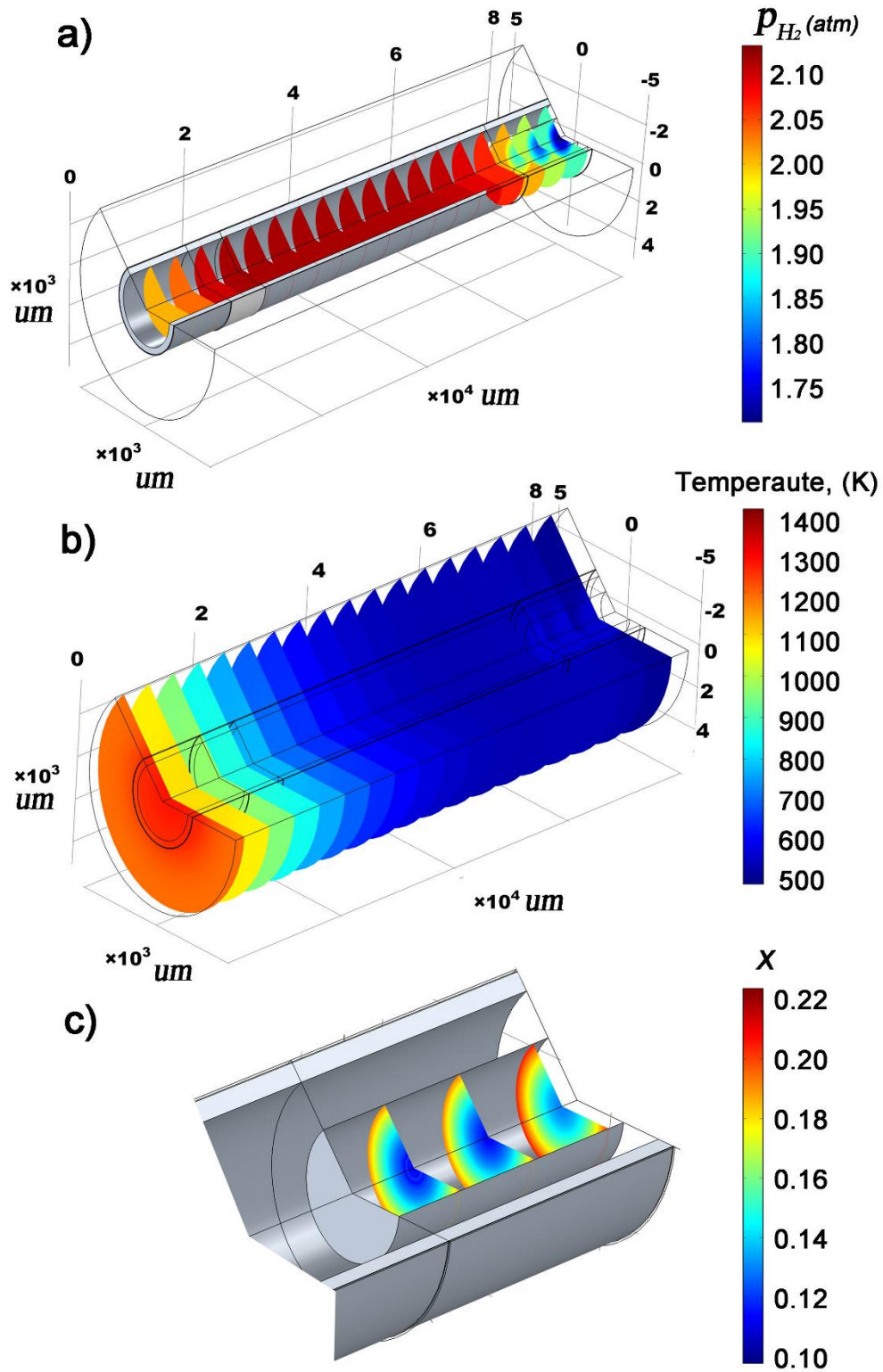


**Fig. 6** Base case simulated results at  $t = 50$  s: a)  $H_2$  partial pressure distribution; b) temperature distribution; c) reacted Mg fraction distribution.

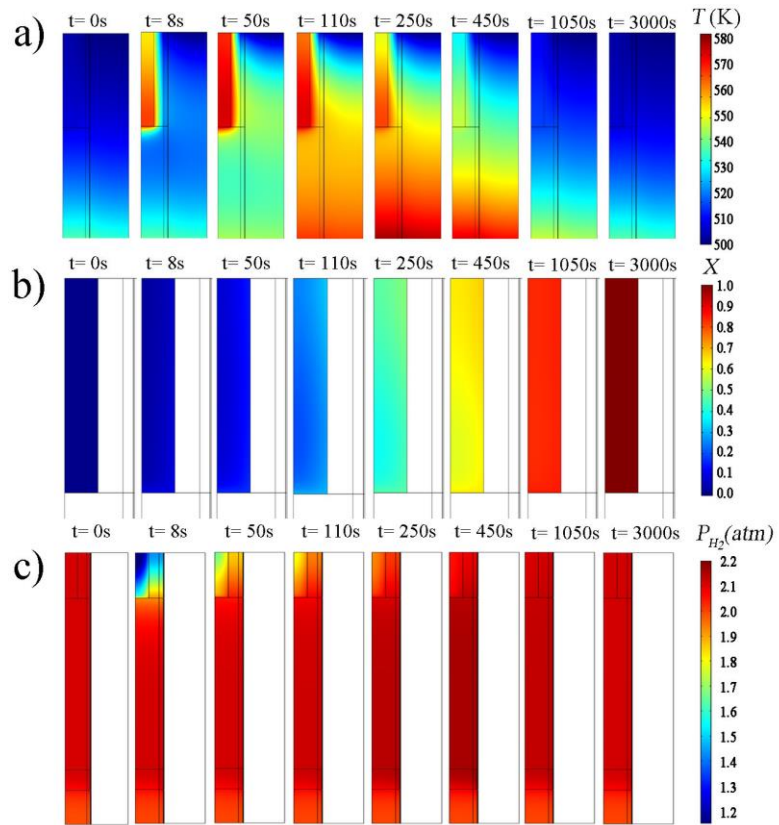


**Fig. 7** Evolution of (a) temperature, (b) reacted Mg fraction, and (c)  $H_2$  partial pressure from 0 s to 3000 s of the base case.

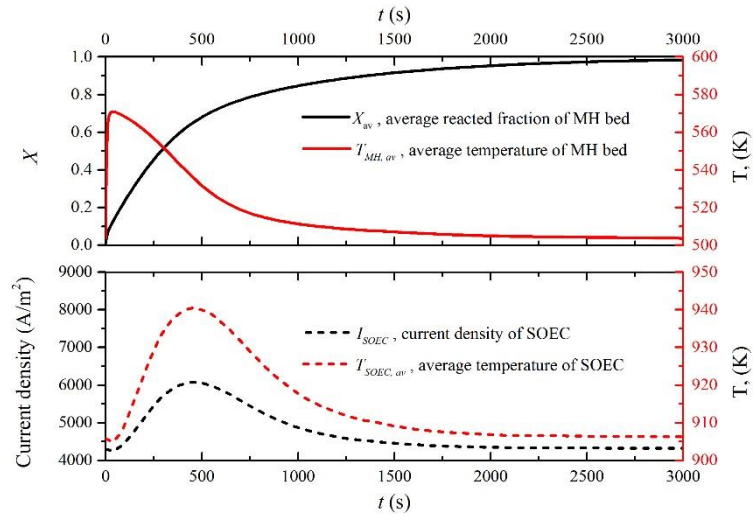


**Fig. 8** The average  $X$  and temperature of the MH bed vs. time (up); the average temperature and current density of SOEC vs. time (down).

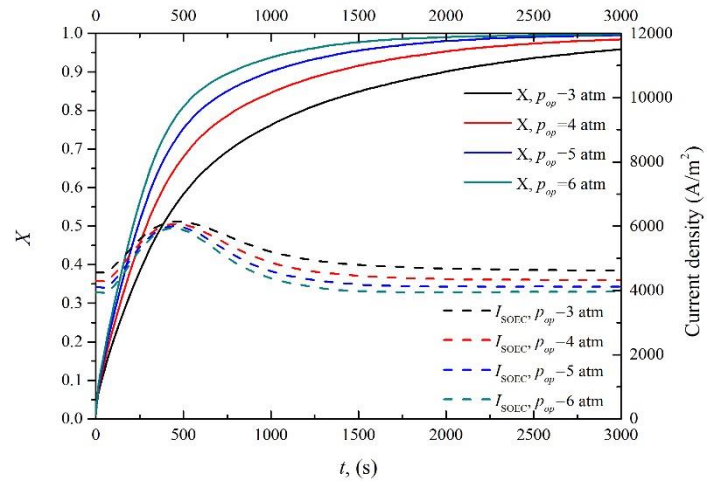


**Fig. 9** Evolution of  $X$  and current density of SOEC section ( $I_{SOEC}$ ) vs. time at different operating pressure.

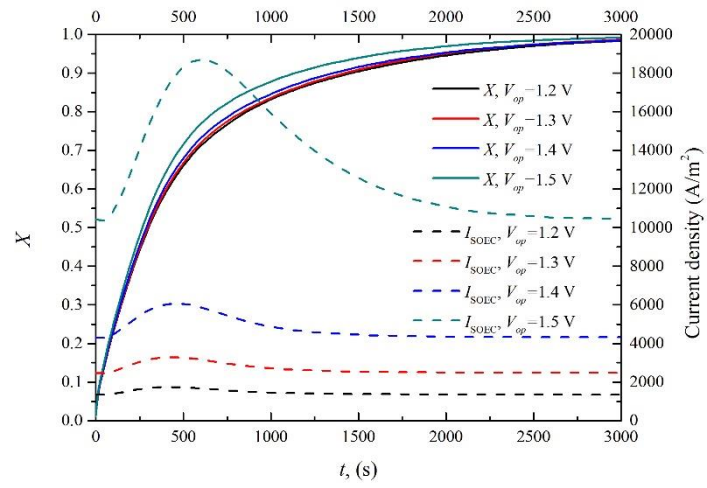


**Fig. 10** Evolution of  $X$  and current density of SOEC section ( $I_{SOEC}$ ) vs. time at different operating voltage ( $V_{op}$ ).

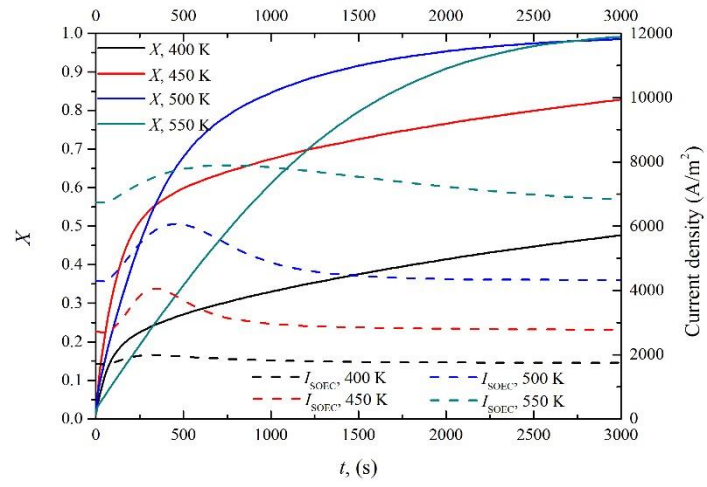


**Fig. 11** Evolution of  $X$  and current density of SOEC section ( $I_{SOEC}$ ) vs. time at different air flow inlet temperature ( $T_{airin}$ ).

## List of Tables

**Table. 1** The geometry parameters of SOEC section and MH section and the operating parameters used in the base case.

**Table. 2** Physical properties of the SOEC materials.

**Table. 3** MH section properties

**Table. 4** Performance summary of the base case

**Table. 5** Summary of sensitivity studies on pressure, voltage and cooling air inlet temperature

**Table. 1** The geometry parameters of SOEC section and MH section and the operating parameters used in the base case.

<b>Parameters</b>	<b>Value</b>
Electrolyser length, $L$	80 mm
Radius of SOEC-MH electrolyser, $r_E$	5.1 mm
<b>SOEC section</b>	
Length, $L_{SOEC}$	16 mm
Radius of SOEC tube radius, $r_{SOEC}$	2.1 mm
Air electrode thickness	30 $\mu\text{m}$
Fuel electrode thickness	308 $\mu\text{m}$
Electrolyte thickness	12 $\mu\text{m}$
<b>MH section</b>	
Length, $L_{MH}$	13 mm
Radius, $r_{MH}$	1 mm
<b>Operating conditions (base case)</b>	
Air inlet temperature, $T_{fuelin}$	1400 K
Fuel inlet temperature, $T_{airin}$	500 K
Operating pressure, $p_{op}$	4 atm
Air flow	23 sccm, Air: H <sub>2</sub> O=1:1 in volume
Fuel flow	40 sccm, N <sub>2</sub> :H <sub>2</sub> =1:1 in volume
SOEC electrolysis voltage, $V_{op}$	1.4 V

**Table. 2** Physical properties of the SOEC materials.

SOEC section parameters	Thermal conductivity ( $\text{W}\cdot\text{m}^{-1}\cdot\text{K}^{-1}$ )	Density ( $\text{kg}\cdot\text{m}^{-3}$ )	Specific heat capacity ( $\text{J}\cdot\text{kg}^{-1}\cdot\text{K}^{-1}$ )	Electrical conductivity ( $\text{S}\cdot\text{m}^{-1}$ )
Ni [29]	71.8	8900	518	$\sigma_{Ni} = \frac{9.5 \cdot 10^7}{T} \cdot \exp\left(\frac{-1150}{T}\right)$
BZCY [30-32]	1.3	6200	407	$\sigma_{BZCY} = 290.4 \cdot \exp\left(\frac{-4600.6}{T}\right)$
SSC[33, 34]	0.6	7500	1960	$\sigma_{SSC} = 100 \cdot 10^{\left(2.12 + \frac{1183}{T} - \frac{4.38 \cdot 10^5}{T^2} + \frac{6 \cdot 10^7}{T^3}\right)}$

**Table. 3** MH section properties

MH section model parameters [36]	Value
Maximum mass content of H of Mg hydride, $wt$	6%
Density of Magnesium hydride powder, $\rho_{MH}$	1800 kg·m <sup>-3</sup>
Effective thermal conductivity of Magnesium powder, $\lambda_{s.MH}$	0.48 W·m <sup>-1</sup> ·K <sup>-1</sup>
Specific heat capacity of Magnesium hydride powder, $c_{p.MH}$	1545 J·kg <sup>-1</sup> ·K <sup>-1</sup>
Reaction rate constant, $k_a$	1·10 <sup>10</sup> s <sup>-1</sup>
Activation Energy, $E_a$	130 kJ
Porosity, $\varepsilon_{MH}$	0.74
Permeability, $\kappa_{MH}$	5.75·10 <sup>-14</sup> m <sup>2</sup>

**Table. 4** Performance summary of the base case

Operating conditions	MH section		SOEC section	
	$p_{op} = 4 \text{ atm}$ $V_{op} = 1.4 \text{ V}$ $T_{airin} = 500 \text{ K}$ $T_{fuelin} = 1400 \text{ K}$	H <sub>2</sub> storage amount (at $t_c$ )	$7.35 \times 10^{-2} \text{ g}$	Average Current density (0 s~ $t_c$ )
Absorption time ( $t_c$ at $X_c = 95\%$ )		1950 s	H <sub>2</sub> production rate	$4.05 \times 10^{-6} \text{ g/s}$
H <sub>2</sub> storage efficiency ( $\eta_{H_2}$ )		55.9%	H <sub>2</sub> O utilization rate	23.7%

**Table. 5** Summary of sensitivity studies on pressure, voltage and cooling air inlet temperature

Unvaried operative parameters	Varied operative parameter	Absorption time, $t_c$ (s)	Storage efficiency (%)	Electrolysis average current till $t_c$ , ( $A/m^2$ )
$V_{op} = 1.4$ V $T_{airin} = 500$ K	$P_{op} = 3$ atm	2790	38%	5049.86
	$P_{op} = 4$ atm	1950	56%	4956.40
	$P_{op} = 5$ atm	1426	76%	4960.41
	$P_{op} = 6$ atm	1109	97%	4994.59
$P_{op} = 4$ atm $T_{airin} = 500$ K	$V_{op} = 1.2$ V	2068	176%	1486.12
	$V_{op} = 1.3$ V	1987	98%	2769.47
	$V_{op} = 1.4$ V	1950	56%	4956.40
	$V_{op} = 1.5$ V	1649	22%	15043.24
$P_{op} = 4$ atm $V_{op} = 1.4$ V	$T_{airin} = 400$ K	>3000	50% ( $X = 0.477$ , $t = 3000$ s)	1808.70 ( $t = 3000$ s)
	$T_{airin} = 450$ K	>3000	52% ( $X = 0.829$ , $t = 3000$ s)	3008.83 ( $t = 3000$ s)
	$T_{airin} = 500$ K	1950	56%	4956.40
	$T_{airin} = 550$ K	2670	31%	6539.38